JOURNAL OF SPACECRAFT AND ROCKETS
Vol. 45, No. 2, March–April 2008

Boundary-Layer Stability Analysis of the Hypersonic International Flight Research Transition Experiments

Heath B. Johnson,* Chris R. Alba,† and Graham V. Candler‡
University of Minnesota, Minneapolis, Minnesota 55455
and
Matthew MacLean,§ Timothy Wadhams,§ and Michael Holden¶
Calspan–University at Buffalo Research Center, Buffalo, New York 14225

DOI: 10.2514/1.31878

Boundary-layer stability analysis is performed by computational fluid dynamics simulation of experiments conducted in the Calspan–University at Buffalo Research Center Large Energy National Shock Tunnel in support of the first flight of the Hypersonic International Flight Research Experimentation program. From the laminar flow solutions, disturbances are calculated using the linear parabolized stability equations method and instability is quantified by integrating the resulting disturbance growth rates. Comparisons are made between the experimentally measured transition locations and the results of the parabolized stability equations analysis. The results show that for the cases tested, the e^N transition correlation works better than the commonly used Re_θ/M_e engineering criterion for predicting the onset of boundary-layer transition from laminar to turbulent flow.

I. Introduction

FOR certain classes of hypersonic cruise vehicles, it is critical for vehicle designers and engineers to know whether the boundary layer at a given flight condition is laminar or if it is expected to transition to turbulence. To estimate whether transition is likely, correlations based on algebraic quantities such as Re_θ/M_e are frequently used because of the relative ease of calculation of the constituent terms. Many different algebraic relations have been evaluated and transition correlations have been developed for specific combinations of geometry and flight conditions [1]. Although these correlations may work to different degrees for predicting transition in cases that are very similar to the tests from which they were developed, they may not be reliably used to predict transition under different freestream conditions or with different body geometries. For example, depending on the specifics of the experiments, the critical value of Re_θ/M_e at transition can range over a factor of three or more, and transition Reynolds numbers calculated by applying this correlation can vary by an order of magnitude [1].

Algebraic correlations can still be useful, for example, in cases where the value of Re_θ/M_e is either very large or very small, and when it and other indicators point to conditions in which a boundary layer will clearly be laminar or turbulent over most of a vehicle. However, in cases where a vehicle spends a significant amount of time at flight conditions where the boundary layer is transitional, it is important to be able to estimate the transition location with greater certainty because errors due to uncertainly of the transition location can dominate the overall uncertainty in the heat transfer rate prediction. This uncertainty can have serious consequences for the design of ballistic and lifting reentry vehicles [2–4], high-speed missiles [5], and hypersonic cruise vehicles [6].

One approach that has shown promise for predicting boundary-layer transition is the application of the parabolized stability equations (PSE) which model the evolution and growth of naturally occurring disturbances within a laminar boundary layer. The PSE provide a physical mechanism-based approach to the calculation of boundary-layer stability and for quantification of the effects of changing body geometry or flight conditions on the boundary-layer stability properties. Although the PSE can be used alone to assess the relative stability or instability of a boundary layer under various conditions, the results of a linear PSE analysis must be coupled with transition correlations based on experimental measurements if we wish to predict the transition location on a vehicle.

The stability and transition analysis for hypersonic boundary layers (STABL) software suite, which has been developed at the University of Minnesota, couples grid generation tools, a two-dimensional/axisymmetric mean flow solver based on the implicit data-parallel line relaxation (DPLR) method [7] and a parabolized stability equation solver, PSE-Chem [8], for efficient analysis of boundary-layer transition problems.

II. Parabolized Stability Equations and the e^N Method

The linearized PSE are derived from the two-dimensional or axisymmetric Navier–Stokes equations where instantaneous flow variables are modeled by a mean plus a fluctuating component. The perturbation on the mean flow state is substituted into the Navier–Stokes equations and the mean flow solution is subtracted, resulting in the disturbance equations. All disturbances are assumed to be small so that terms which are nonlinear in the disturbances can be neglected. The disturbances are modeled as a fast-oscillatory wave part and a slowly varying shape function, and solution of the PSE yields the spatial evolution of disturbances at a particular frequency in the boundary layer. More details about the PSE approach as implemented here can be found in [8].

A mechanism-based transition correlation that works well with the PSE approach is the e^N method, in which N represents the integrated growth rate of unstable boundary-layer disturbances:

$$N(\omega, s) = \int_{s_0}^{s} \sigma \, \mathrm{d}s$$

Presented as Paper 311 at the 45th AIAA Aerospace Sciences Meeting and Exhibit, Reno, NV, 8–11 January 2007; received 30 April 2007; revision received 27 August 2007; accepted for publication 28 August 2007.

*Senior Research Associate, Department of Aerospace Engineering and Mechanics. AIAA Senior Member.
†Second Lieutenant, U.S. Air Force, Research Assistant, Department of Aerospace Engineering and Mechanics. AIAA Student Member.
‡Professor, Department of Aerospace Engineering and Mechanics. AIAA Associate Fellow.
§Senior Research Scientist, Aerothermal/Aero-optics Evaluation Center. AIAA Member.
¶Program Manager, Aerothermal/Aero-optics Evaluation Center. AIAA Fellow.

where ω is the frequency of a disturbance, s is the distance along the surface, s_0 is the location of the first critical point, and σ is the disturbance growth rate, defined as

$$\sigma = -Im(\alpha) + \frac{1}{2E}\frac{dE}{ds}$$

In this equation, α is the complex streamwise wave number, and E is the disturbance kinetic energy, defined as

$$E = \int_n \bar{\rho}(|u'|^2 + |v'|^2 + |w'|^2)\,\mathrm{d}n$$

where $\bar{\rho}$ is the mean flow density, (u', v', w') are the complex fluctuating velocity components, and n is the physical direction normal to the body surface.

Despite the assumptions made in this approach, the e^N method has shown promising agreement with experiment [9]. Using linear stability theory (LST) or PSE to compute N factors for specific cases for which experimental data is available, the value of N at transition has been shown to be about 8–11 for many different smooth-body geometries in low-disturbance freestream conditions [10–12]. In general, N factors from PSE analysis may be larger than those found from the quasi-parallel LST [13]. The influence of factors such as body roughness and higher levels of freestream noise are manifested in lower values of N, and values of around 5.5 have shown good correlation with the onset of transition in noisier environments such as conventional wind tunnels or shock tunnels [13–16]. The effects of facility freestream noise and other factors can be seen, for example, in comparisons of flared cone models in conventional and quiet tunnels where the N factor at transition was found to range from 3.8–7.8 [13].

III. Description of Experiments

Although application of linear stability theory, together with the e^N transition correlation, has been found to work fairly well for a variety of conditions where the environmental noise is generally low, the accuracy of many high-speed e^N computations remains uncertain, for it is often not clear whether bluntness effects, wall temperature distributions, and so on were handled with sufficient accuracy [17]. To make a careful comparison with PSE, detailed information about the geometry and flight conditions is required.

One of the goals of the Hypersonic International Flight Research Experimentation (HIFiRE) program is to provide high-quality data for boundary-layer stability analysis. [The HIFiRE program was previously known as the U.S. Air Force Research Laboratory's Fundamental Research in Hypersonics (FRESH) program.] The experimental data presented here were generated from experiments performed in support of the first HIFiRE flight using the Calspan–University at Buffalo Research Center (CUBRC) Buffalo Research Center Large Energy National Shock Tunnel (LENS_1). The flight experiment will be at Mach 7, and test conditions for the experiments which were simulated are shown in Table 1. In addition, experimental data are also available for a number of related tests performed at Mach 10, and those conditions are listed in Table 2.

Table 1 Test conditions for the Mach 7 HIFiRE/FRESH experiment simulations

Test conditions	Units	Run 4	Run 5	Run 7	Run 8
H_0	MJ/kg	2.08	2.62	2.62	2.09
M_∞	——	6.58	7.14	7.15	6.58
T_∞	K	213.0	231.8	231.1	214.0
ρ_∞	kg/m^3	0.12504	0.06957	0.07060	0.12568
Re_∞	1/m	1.66e + 7	9.76e + 6	9.92e + 6	1.67e + 7
u_∞	m/s	1928	2184	2185	1933
T_{wall}	K	300.1	299.3	301.0	301.3
Nose radius	mm	2.5	2.5	5.0	5.0

The geometry for all test cases was a 7 deg half-angle cone with either a sharp or blunt nose, and three different nose radii were tested. The model for the Mach 10 tests was a 2.3 m cone, whereas the Mach 7 model was conical up to approximately 1.1 m, after which it was cylindrical. All Mach 7 transition measurements were made on the conical section. Experimental results which were provided** [18] consisted of wall heat transfer rates from gauges traversing the length of the body on four rays: 0, 90, 180, and 270 deg, and the consistency of the measured heat transfer rates across the rays verifies that the cone was oriented at zero degree angle of attack. The Mach 7 runs (4, 5, 7, 8) were performed using a cone which was instrumented with a lower spatial resolution compared with the other runs, yielding a larger uncertainty in transition locations for these runs compared with the others.

IV. Mean Flow Solutions

Laminar mean flows for all the test cases were generated using an optimized two-dimensional/axisymmetric mean flow solver based on the implicit data-parallel line relaxation method [7] which is provided with STABL. The solver produces second-order accurate laminar flow solutions with low dissipation and shock capturing.

For each of the simulations, 360 × 360 point structured grids were generated with clustering both at the body surface and at the nose. Because recent versions of STABL include functions for automatic grid tailoring based on the methods used in the NASA OUTBOUND code [19], grid tailoring was used for the Mach 7 blunt body cases to generate grids where the outer boundary closely followed the shock and the wall spacing met the desired criteria. For the Mach 10 simulations, which were performed before the grid tailoring feature was implemented, the outer grid shape was carefully generated by hand to follow the shock.

To ensure that the boundary-layer solutions were well resolved, grid point clustering in the body-normal direction was adjusted to obtain values of y^+ less than unity at the first solution point away from the wall. This typically resulted in approximately 100 grid points within the boundary layer. To minimize errors, clustering of grid points along the body surface was controlled using multiple segments to obtain monotonically increasing grid point spacing, with moderate stretching of less than 4%. With this, the largest streamwise grid spacing, which was reached at the end of the body, was typically around 5–6 cm. Grid resolution studies for similar geometries and freestream conditions have shown that these combined criteria result in a mean flow solution and subsequent PSE results which are grid-resolved [16,20,21].

Table 2 Test conditions for the Mach 10 experiment simulations

Test conditions	Units	Run 18	Run 19	Run 20	Run 21	Run 22
H_0	MJ/kg	4.49	4.44	4.47	4.56	4.42
M_∞	——	9.91	9.95	9.92	9.93	10.04
T_∞	K	206.71	203.35	205.41	209.33	198.62
ρ_∞	kg/m^3	0.0121	0.0119	0.0123	0.0160	0.0089
Re_∞	1/m	2.52e + 6	2.51e + 6	2.57e + 6	3.33e + 6	1.92e + 6
T_{wall}	K	295.61	295.22	296.61	299.00	297.28
Nose radius	mm	6.35	2.50	sharp	6.35	sharp

**T. P. Wadhams, private correspondence, 2006.

The governing equations for both the DPLR and PSE-Chem solvers are the Navier–Stokes equations extended for a gas mixture with ns species. A two-temperature model is used where the energy in the translational and rotational modes is characterized by the translational temperature T, and the energy of the vibrational modes is characterized by the vibrational temperature T_v. Closure of the governing Navier–Stokes equations is obtained through relations for the transport of mass, momentum, and thermal energy due to gradients of mass concentration, velocity, and vibrational and translational temperature, respectively. The species diffusion velocity is given by Fick's law of mass diffusion. The mass diffusion coefficient D is found from assuming a constant Schmidt number of 0.5 which is the same for all species.

Species viscosities are specified in a general fashion, so that different viscosity models may be used through specified temperature ranges, and blending functions are used to maintain smooth function values and derivatives between models. The species translational conductivity is computed by Eucken's relation. The gas mixture viscosity and conductivity are found from the Wilke mixing law. More details are available in [8].

V. Parabolized Stability Equations Analysis

The PSE-Chem code which was used for these calculations solves the parabolized stability equations for supersonic and hypersonic applications, including effects of finite rate chemistry and translational–vibrational energy exchange, to predict the growth rate of naturally occurring disturbances in hypervelocity flows. PSE-Chem is implemented using message passing interface (MPI) for efficient distribution of calculations which were run on a Linux cluster. The STABL suite which was used for this work provides a graphical user interface and an object-oriented scripting interface to PSE-Chem, to easily run all the cases that are required for the stability analysis of a boundary layer. Additional details can be found in [8].

Estimates of the most unstable disturbance frequencies are found from analysis of the mean flow profiles. First-mode disturbance frequencies are estimated based on the boundary-layer thickness and edge velocity[††]:

$$\omega = \frac{u_e}{10\delta}$$

whereas the frequencies of second- and higher-mode disturbances, which represent constrained acoustic waves, are more accurately estimated using an integral method [22].

The PSE are solved in an identical fashion whether the resulting disturbances are characterized as first-mode or second-mode. Because it is known that first-mode disturbances are most unstable for oblique waves, and second-mode disturbances are most unstable for two-dimensional waves, we need to test our PSE results to determine which mode is dominant for a specific case. Using the PSE planner in STABL, we cover both the estimated first- and second-mode disturbance frequencies with test points for two-dimensional disturbance waves, and if first-mode disturbances are found to be the most unstable in the results, we add test points for oblique waves (helical in axisymmetric flows).

The PSE-Chem test matrix for run 21 is shown in Fig. 1. This is typical of the PSE analyses which were run, in which 2000 combinations of disturbance frequencies and starting locations were evaluated in approximately 25 min on a Linux Opteron cluster. The raw PSE results can be seen in Fig. 2a, which shows N-factor curves for each of the PSE test cases. Each family of curves in the plot represents a disturbance at a given frequency, where the starting location for the disturbance is varied to determine the upstream critical point resulting in the largest subsequent N factor. From the collected PSE N factors, we can extract the envelope of the maximum N factors and corresponding disturbance frequency that are reached at each surface location. These results are shown in Fig. 2b. The waviness of the maximum N factor and the frequency at maximum N-factor curves is a result of using a finite number of discrete

[††]Steven P. Schneider, private correspondence, 2004.

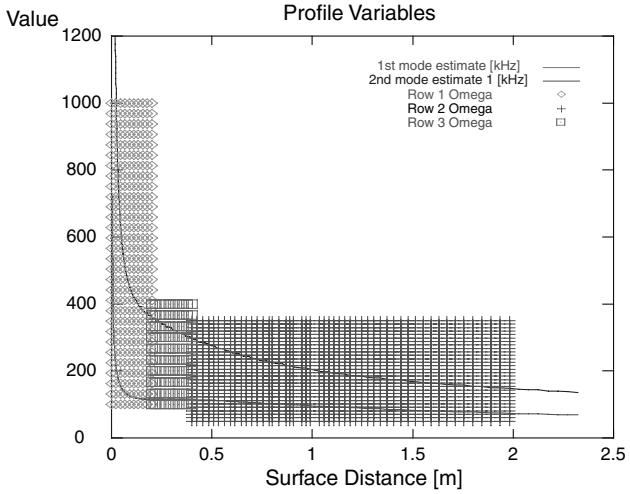

Fig. 1 PSE-Chem test matrix for run 21. The y axis is estimated disturbance frequency.

frequencies for the stability analysis. Although increasing the frequency resolution would result in smoother curves, it is possible to extract the envelope of maximum values from the present results. The flat areas on the frequency of maximum N-factor curve indicates that a single frequency, from those that were tested, is most unstable over some region of the body.

VI. Results and Discussion

A. Disturbance Mode Analysis

Figure 2b shows the estimated first- and second-mode disturbance frequencies along with the results of the PSE analysis for run 21. Considering the curve of the most amplified disturbance frequency, the downstream shift of the curve found from the PSE results, relative to the estimated disturbance frequency, is a result of the fact that a given frequency of disturbance is unstable over a certain portion of the body: the width of the unstable region in an s vs growth rate stability diagram. Therefore, the PSE results of the most unstable disturbance frequency, as seen in Figs. 2b and 3b, are in some sense indicating the downstream critical point of the stability diagram at a given frequency.

This test case, run 21, is for a blunted cone, and we see that from the nose until approximately $s = 0.16$ m (25 nose radii) downstream, the frequency of the disturbances which produce the maximum N factors corresponds to the estimated first-mode frequency. Disturbances originating in this region continue to grow slowly over the rest of the body, as seen in Fig. 2a. At a surface distance of $s = 0.5$ m (78 nose radii), second-mode disturbances begin to dominate and they continue to be unstable over the rest of the body.

For the sharp cone cases, for example run 22, only second-mode disturbances are the most unstable, of the two-dimensional disturbances that were tested, as seen by comparing the frequencies in Fig. 3. Although it is possible that oblique first-mode disturbances may still have growth over some portion of the body, the largest N factors are clearly generated by second-mode disturbances. Because the results for the other sharp- and blunt-nose cases are similar to that shown here, we focus on only two-dimensional (axisymmetric) disturbances in our PSE analysis.

B. Effect of Chemistry

An advantage of performing numerical simulations is that we can selectively turn on or off certain parts of the models to test their influence on the overall solution. Here, we study the effect of chemistry and molecular vibrational excitation in both establishing the mean flow and in the calculation of boundary-layer disturbance growth rates. To do this, we begin by choosing the highest-enthalpy case of the tests which were simulated, run 21 at 4.56 MJ/kg, because chemistry effects in all other tests will be smaller. The laminar mean flow is first calculated both with and without chemistry

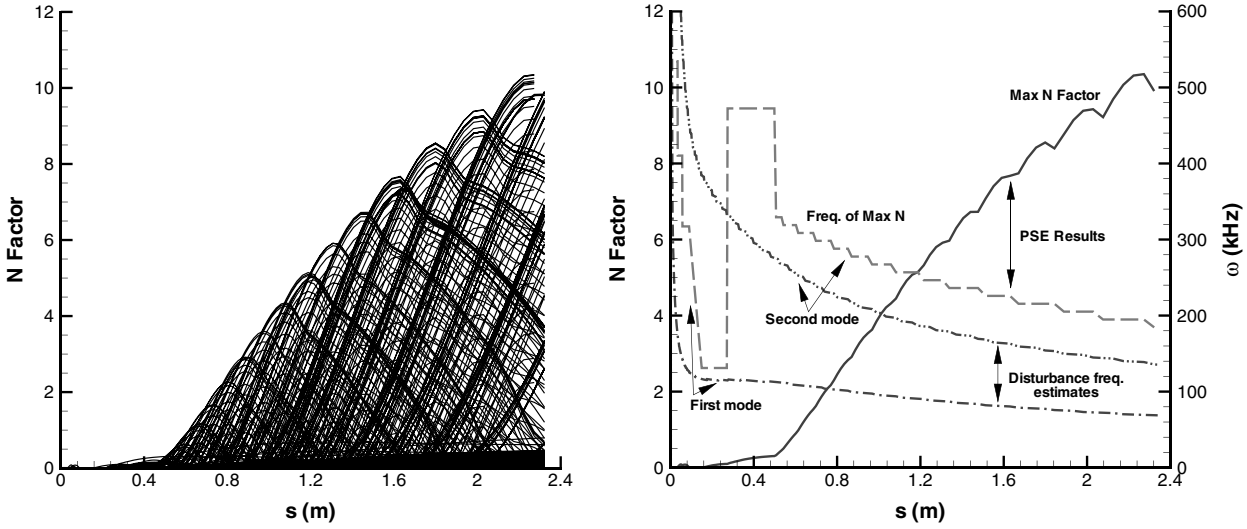

a) Raw PSE *N* factor results

b) Comparison of estimated and calculated most-unstable disturbance frequencies

Fig. 2 PSE Results for blunt cone run 21.

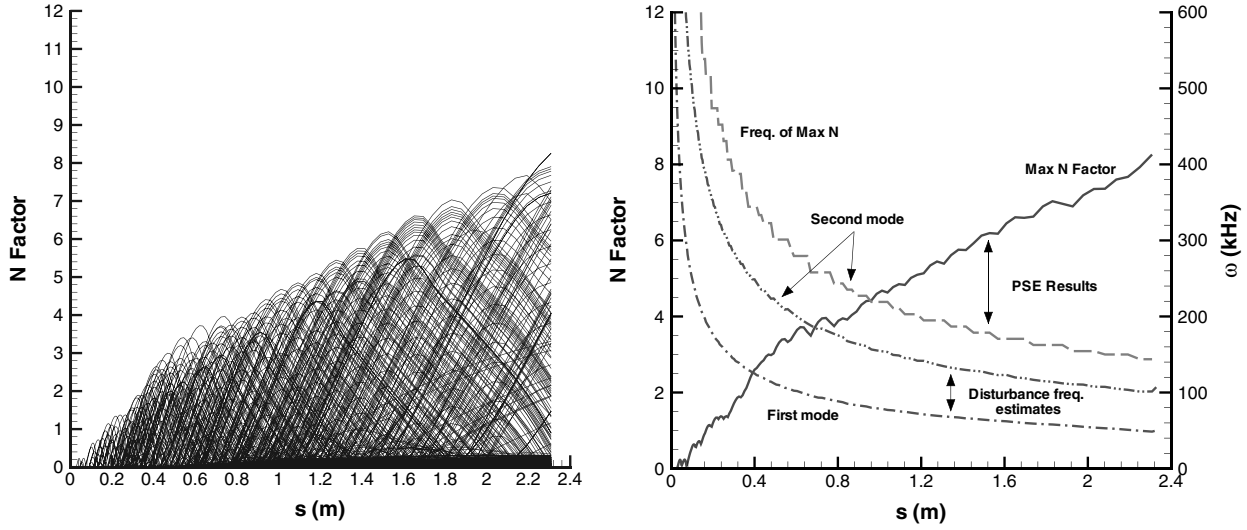

a) Raw PSE *N* factor results

b) Comparison of estimated and calculated most-unstable disturbance frequencies

Fig. 3 PSE Results for sharp cone run 22.

and vibrational effects. At this low enthalpy, the effects are slight but can be seen, for example, in the boundary-layer temperature profiles shown in Fig. 4. Although there is only a small difference in the temperature profiles between the reacting and nonreacting mean flows, the model predicts a significant amount of thermal nonequilibrium, as seen in Fig. 4b.

Next, we tested the influence of chemistry in the disturbances by running PSE-Chem on both the reacting and nonreacting mean flow solutions. By doing this, we can determine whether chemistry effects on the overall boundary-layer stability are primarily the result of changes to the laminar mean flow profiles or if chemistry and vibrational excitation caused by the disturbances themselves plays an important role. *N* factors for all the cases are shown in Fig. 5a. As with all the blunt-nose cases, we see slowly growing first-mode disturbances beginning at the nose, along with more rapidly growing second-mode disturbances beginning farther along the body. Because differences between the reacting and nonreacting cases are slight, they are difficult to discern in this figure.

A close-up of the results at a frequency of 247 kHz is shown in Fig. 5b. Compared with the nonreacting case, including the effects of chemistry and vibration results in slightly higher *N* factors and, therefore, a boundary layer which is more unstable. In either case, the effect of including chemistry and vibration in the disturbances is slightly stabilizing, resulting in lower *N* factors. Although chemistry effects are very small for the current tests as a result of the low freestream total enthalpy, the results are consistent with what we have previously found in the analysis of boundary layers over cones in high-enthalpy flows [16]. Chemistry effects may be found to be more significant under other test conditions.

C. Comparison of Re_θ/M_e and Parabolized Stability Equations *N*-Factor Correlations

Figures 6–8 show the experimentally measured wall heat flux together with the heat flux calculated for each run using STABL. For the sharp cone tests, the measured and computed wall heat fluxes agree very well in the laminar region. For the blunt-nose cases, the small bluntness (run 19, $r_n = 0.250$ cm) simulation predicted heat transfer rates very close to the experimental values, whereas the larger bluntness cases (runs 18 and 21, $r_n = 0.635$ cm) showed some differences, especially near the nose. It is not clear at this point what causes this difference. The plots clearly show a characteristic rise in heat flux due to transition. The transition process is more rapid in the Mach 7 cases, with a sudden departure of the measured heat flux from the computed laminar curve. In these cases, the location of transition

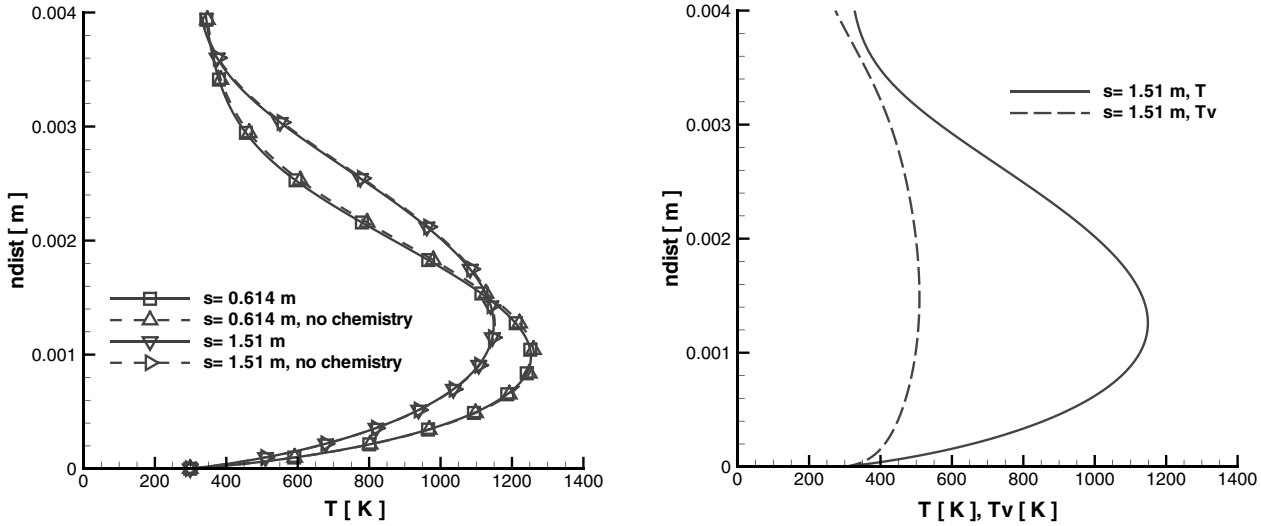

a) Boundary-layer temperature profiles with and without chemistry **b) Temperature profiles with and without vibrational energy modeling**

Fig. 4 Effect of chemical and thermal nonequilibrium modeling for run 21.

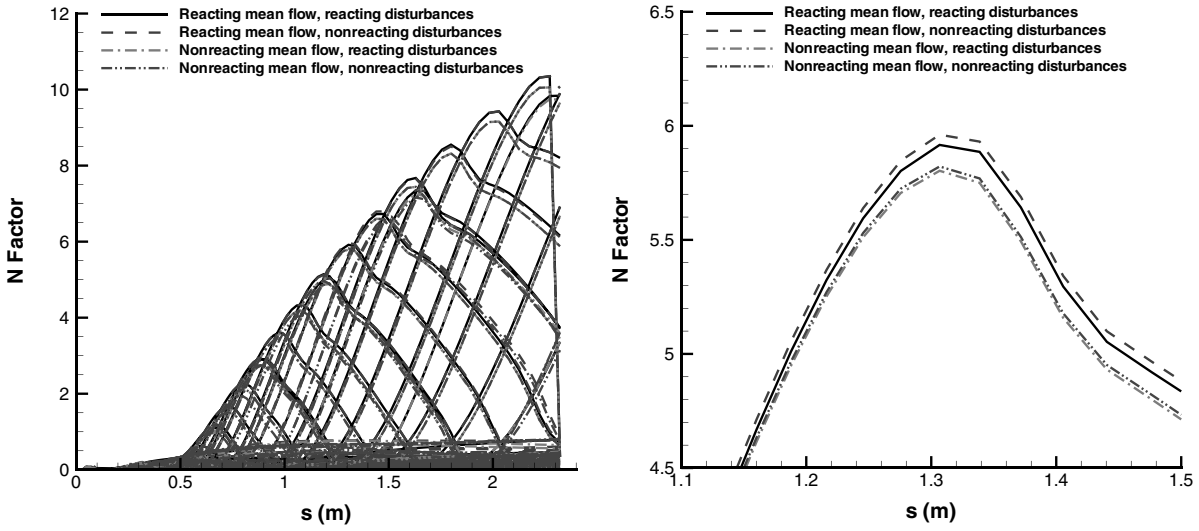

a) Most-amplified *N* factors for each test frequency **b) Closeup of results of 247 kHz**

Fig. 5 Effect of chemical and thermal nonequilibrium modeling on the *N* factors for run 21.

is fairly unambiguous, whereas for the Mach 10 cases, it is more difficult to pinpoint a specific transition location. When transition begins, the experiments show a highly intermittent flow with turbulent regions mixed with laminar flow [18]. Thus, it is difficult to precisely define the transition location.

Two methods are commonly used for defining the location of transition onset from heat transfer data: either selecting the first location where the heat transfer data departs from the laminar value or by finding the intersection of straight lines, on a logarithmic plot, drawn through the laminar and transitional portions of the data. In some cases, it is very easy to pick a transition location from the experimental results because there is a sharp increase in the wall heat flux from the laminar value. For other runs, the transition from laminar flow is more gradual and one could arguably pick a range of surface locations as the transition point.

From the experimental data, the range of transition locations for each run was extracted by selecting the range of surface locations where a rise in wall heat flux, relative to the laminar value, was detected. Figure 9 shows an example of this, in which the measured and calculated wall heat flux for run 4, along with the calculated N factor, are plotted. The surface locations bracketing the onset of transition are marked, as well as the corresponding values of N. Because of the limited number of heat flux gauges, the transition location cannot be determined more accurately than shown. This results in a range of values of Re_θ/M_e and N factor indicating the uncertainty in these values at transition due to the uncertainty in the transition location.

The values of N and Re_θ/M_e at the bracketed transition locations are listed in Table 3. In these data, the relatively larger spread in the transition values of Re_θ/M_e or N for a given test at Mach 7 compared with Mach 10 is due to the larger spacing between heat transfer gauges on the model used in the Mach 7 experiments. Based on these results, a transition correlation of $N = 5.5$ was selected. The location where the N factor first reaches a value of 5.5 is marked on each of the plots in Figs. 6–8, which indicate that the e^N method with $N = 5.5$ does an excellent job of correlating the measured transition location for each of the tests, regardless of freestream Reynolds or Mach numbers or the nose bluntness.

Figure 10a shows a plot of the value of M_e and Fig. 10b shows Re_θ/M_e for each of the runs. The values of Re_θ/M_e at transition vary by a factor of three over the different runs, and clear variations in the critical value can be seen with changes in both Mach number and nose bluntness.

The fact that a transition criterion based on Re_θ/M_e is not able to resolve differences in transition location with changes in nose bluntness can be seen by comparing the results from run 4 with run 8, or by comparing run 5 with run 7. Table 1 shows that, for these groupings, the freestream conditions are approximately the same but

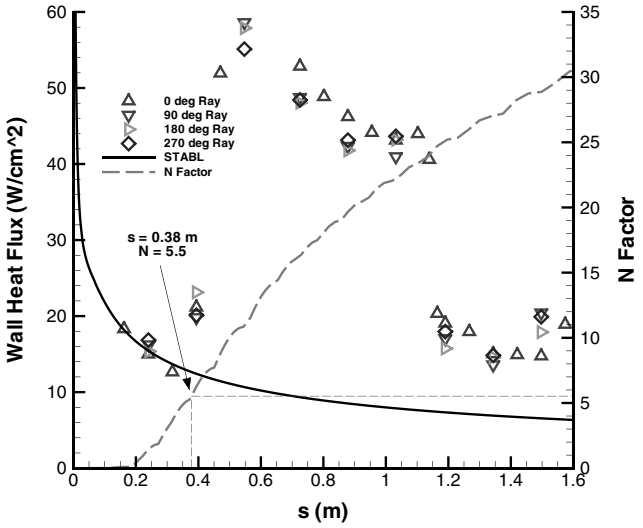

a) Run 4, r_n = 2.5 mm, $Re_\infty = 1.66\times10^7$/m

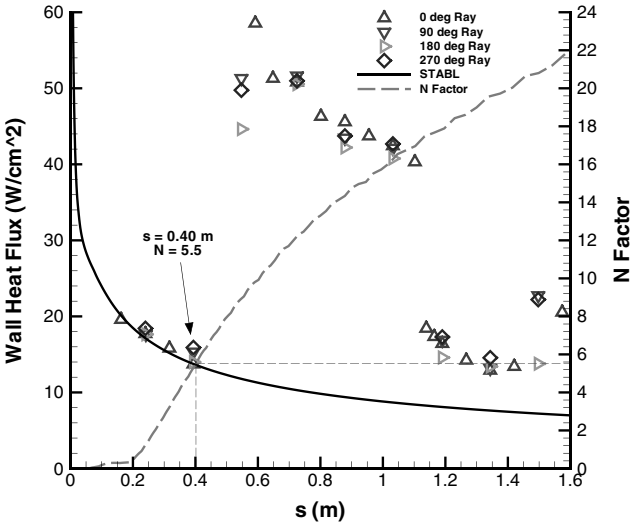

b) Run 5, r_n = 2.5 mm, $Re_\infty = 9.76\times10^6$/m

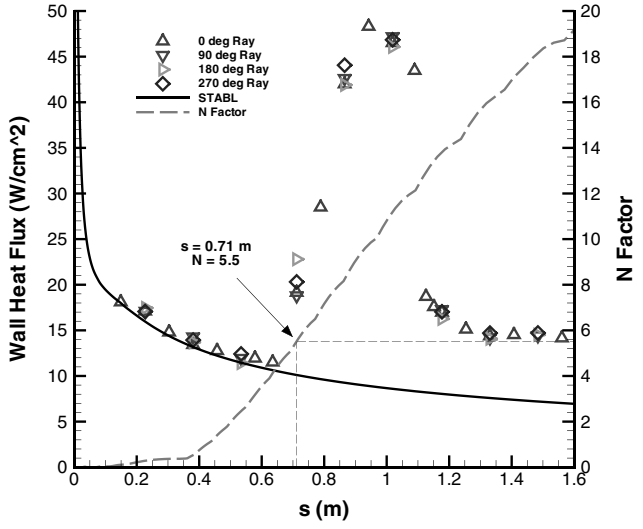

c) Run 7, r_n = 5.0 mm, $Re_\infty = 9.92\times10^6$/m

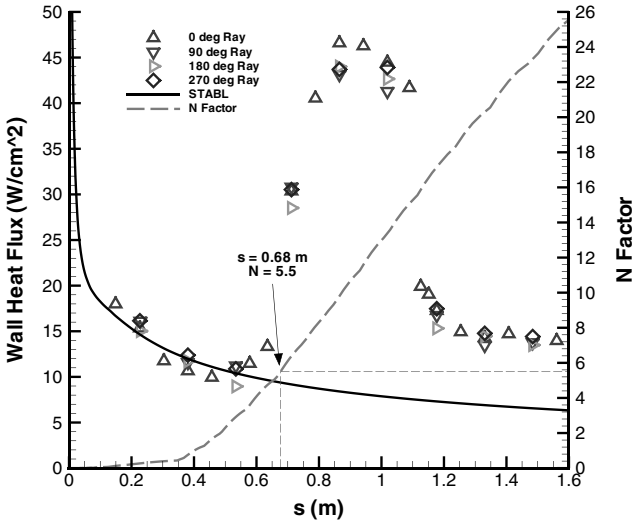

d) Run 8, r_n = 5.0 mm, $Re_\infty = 1.67\times10^7$/m

Fig. 6 Comparison of STABL predictions and experimental results for the Mach 7 runs. The $N = 5.5$ point is shown only for reference.

the nose radius is varied between 2.5 and 5.0 mm. For a given freestream condition, the Re_θ/M_e plot does not change appreciably with nose bluntness, as seen in Fig. 10b. However, the experimentally measured transition location shows a large shift, as seen in Fig. 6. Therefore, the critical value of Re_θ/M_e also shifts with nose bluntness, and no single value correlates with the transition location.

The values of Re_θ/M_e at transition, shown in Fig. 11a, exhibit approximately a factor of three variation between the lower and higher Mach number tests, and a larger scatter in the results even within tests at the same Mach number. In addition, the value of Re_θ/M_e at transition shows a strong variation with unit Reynolds number. The value of Re_θ/M_e at transition also changes with nose bluntness, as indicated in the figure.

In contrast, the results in Fig. 11b show that the value of the N factor at transition is clearly clustered around $N = 5.5$ for all the cases, with a wider range of uncertainty for the Mach 7 (higher unit Reynolds number) runs because of the lower spatial resolution of the heat transfer gauges on the cone used for these tests, and the fact that N grows very rapidly with increasing surface distance in these cases. This rapid growth for the Mach 7 runs can be seen in Figs. 6 and 9 as the large slope of the N-factor curves.

The question of importance to engineers and designers is whether either method does a reasonable job of predicting boundary-layer transition. Despite the apparently large range of uncertainty in the N factors at transition, seen in Fig. 11b, comparison with Figs. 6–8 show that a transition correlation of $N = 5.5$ does an excellent job in matching the measured transition locations across all the tests. To better illustrate this, we choose typical transition values of $Re_\theta/M_e = 150$ and $N = 5.5$, and we plot predicted vs measured transition Reynolds numbers for each test. The results are shown in Fig. 12. If the predicted and measured transition locations agree, the data points should fall along a straight line.

For these tests, a fixed value of N correlates the measured transition location very well, whereas a fixed value of Re_θ/M_e shows no correlation. Although an argument could be made that some other curve fit should be used for the Re_θ/M_e transition correlation, that is not a sufficient solution because transition values of Re_θ/M_e may vary with many freestream and geometry parameters. In contrast, using stability theory to capture the physics of the transition process results in a more useful transition correlation.

D. Extrapolating Ground Test Results to Flight

It should be emphasized that the value of $N = 5.5$, which was found to correlate transition in the cases studied here, is valid only for wind-tunnel experiments. For flight experiments, a higher value of $N = 8$–11, is usually found to correlate the measured transition location. The difference in the values of N at transition is a function of the difference in freestream noise levels in the test environments.

Therefore, to extrapolate the results of ground test transition experiments to flight, we can estimate transition as the location where

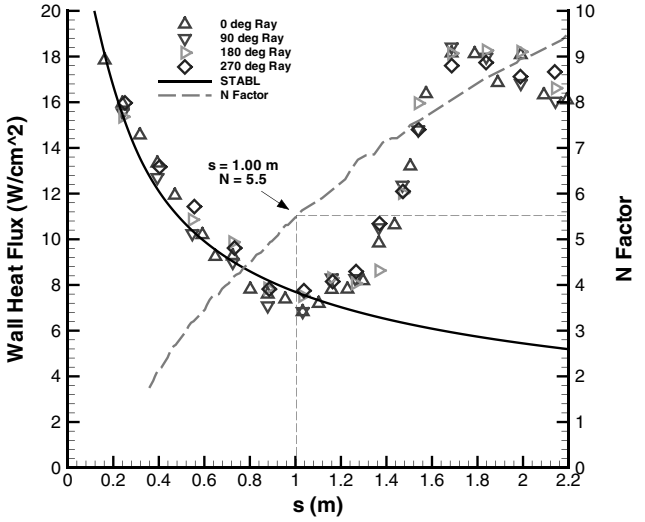

a) Run 19, r_n = 2.50 mm, $Re_\infty = 2.51\times10^6$/m

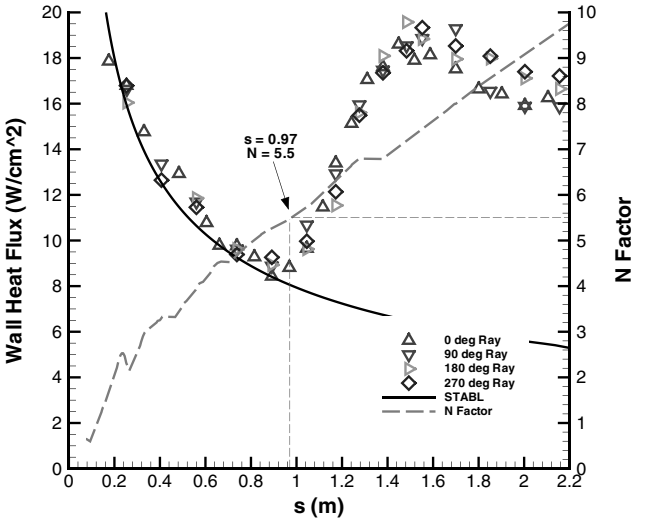

b) Run 20, sharp cone, $Re_\infty = 2.57\times10^6$/m

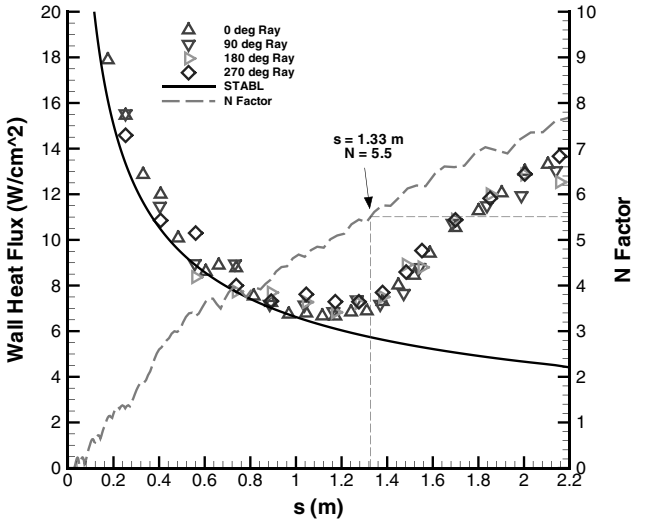

c) Run 22, sharp cone, $Re_\infty = 1.92\times10^6$/m

Fig. 7 Comparison of STABL predictions and experimental results for the Mach 10 runs. The $N = 5.5$ point is shown only for reference.

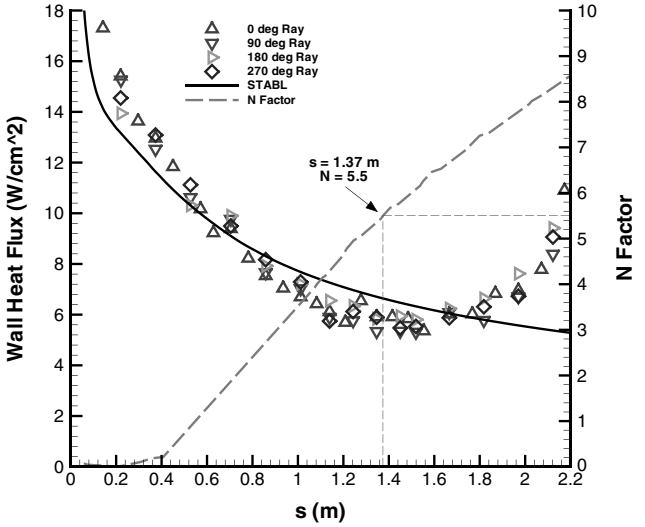

a) Run 18, r_n = 6.35 mm, $Re_\infty = 2.52\times10^6$/m

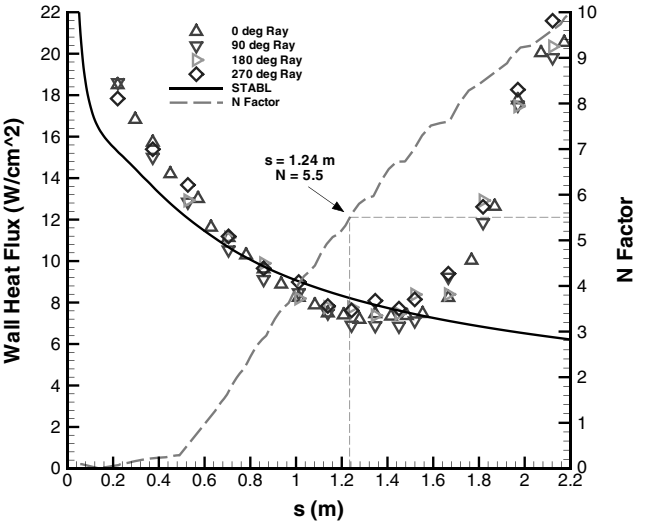

b) Run 21, r_n = 6.35 mm, $Re_\infty = 3.33\times10^6$/m

Fig. 8 Comparison of STABL predictions and experimental results for the Mach 10 runs. The $N = 5.5$ point is shown only for reference.

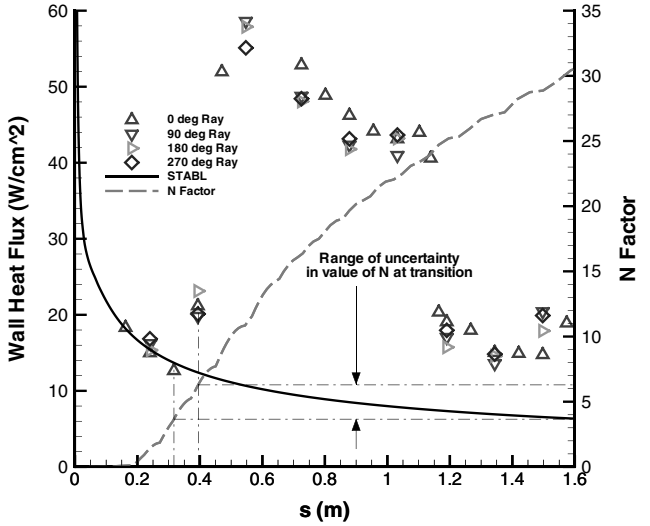

Fig. 9 Measured and calculated wall heat flux for run 4 along with the calculated N factor. The surface locations bracketing the onset of transition are marked, as well as the corresponding values of N.

a higher value of N is reached, for example, $N = 10$, assuming that the relevant freestream conditions are matched. The change in the transition location in flight, compared with what is measured in a ground test experiment, is a function of the slope of the N-factor curve and therefore an indication of the sensitivity of the boundary layer to the factors affecting transition.

Using STABL, a researcher can also analyze the changes in boundary-layer stability and estimated transition location due to the effects of wall temperature distribution and freestream conditions, which, for a vehicle in flight, may differ from the values in a ground test experiment.

VII. Conclusions

In this paper, we used heat transfer data from nine different CUBRC LENS shock-tunnel experiments to compare the measured boundary-layer transition location with the results of PSE calculations for both sharp and blunt cones. Using the STABL stability and transition software suite, we were able to generate high-quality computational fluid dynamics mean flow and PSE solutions. The PSE method, coupled with the semi-empirical e^N-transition correlation using $N = 5.5$, was found to work very well in all of the

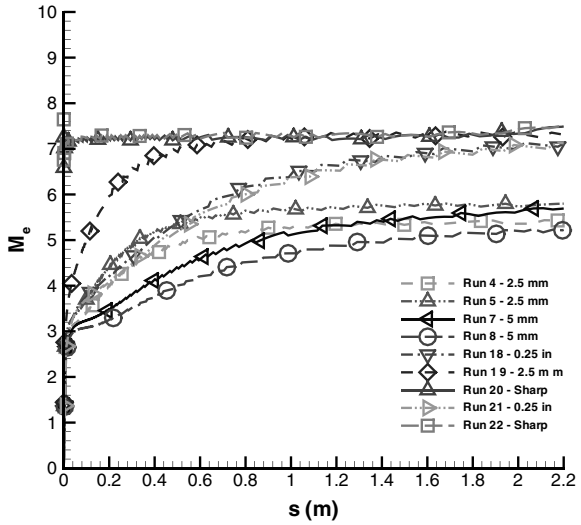

a) Edge Mach numbers

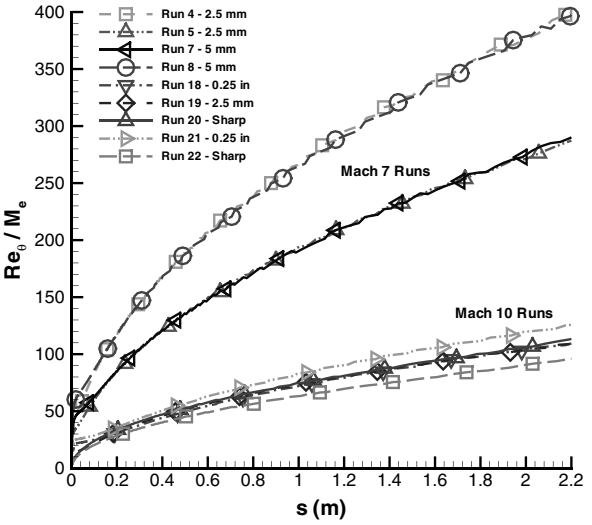

b) Values of Re_θ/M_e

Fig. 10 Edge Mach number and Re_θ/M_e for each run.

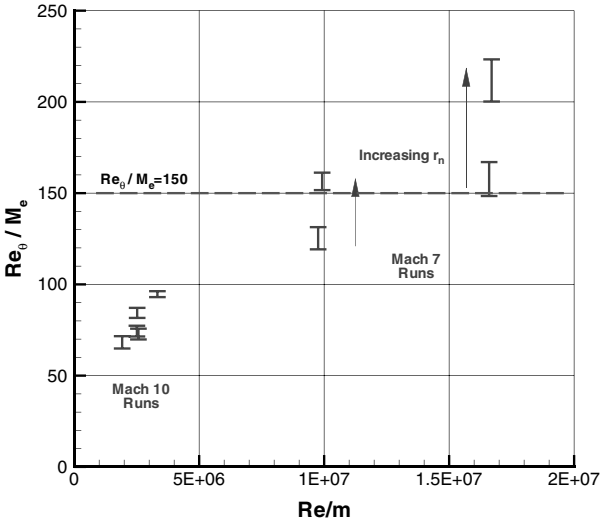

a) Range of values of Re_θ/M_e at transition

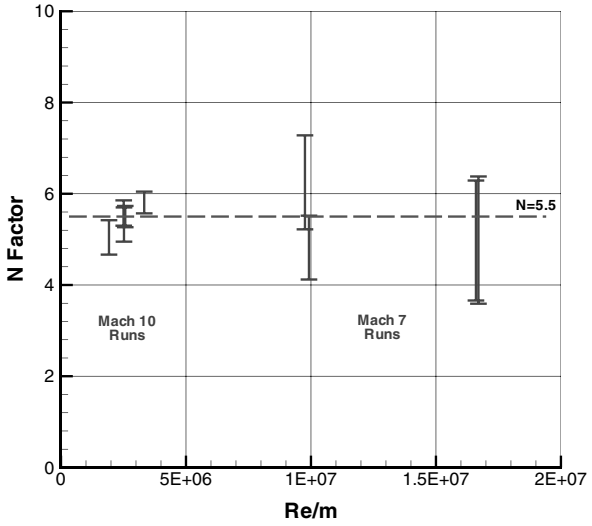

b) Range of N factors at transition

Fig. 11 Range of Re_θ/M_e and N factors at the measured transition locations as a function of freestream unit Reynolds number. The uncertainty bars indicate the variation in the respective quantities to the uncertainty in defining the transition location for each run.

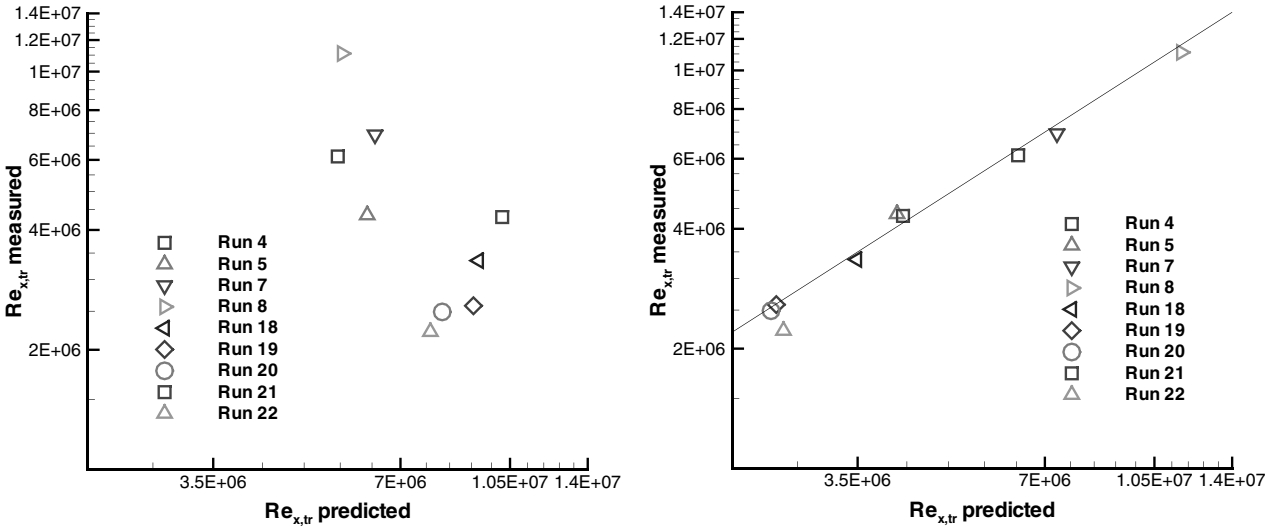

Fig. 12 Comparison of predicted and measured transition Reynolds numbers.

cases. Agreement between measured and predicted transition locations was very good for both the Mach 7 and Mach 10 runs, as well as for both sharp-nose and blunt-cone geometries with a range of values of nose bluntness. In contrast, the values of Re_θ/M_e at the transition locations varied with both Mach number and nose bluntness by approximately a factor of three across the different tests. This provides an additional validation of the coupled PSE and e^N methods for predicting boundary-layer transition locations on both sharp and blunt cones for Mach numbers between 7 and 10.

Acknowledgments

Work at the University of Minnesota was sponsored by Sandia National Laboratories Award #619327 and by the U. S. Air Force Office of Scientific Research under grant #FA9550-04-1-0341. Work at Calspan–University at Buffalo Research Center was sponsored by the U.S. Army Research Development and Engineering Command under Contract #DAAH01-98-C-R196. The views and conclusions contained herein are those of the authors and should not be interpreted as necessarily representing the official policies or endorsements, either expressed or implied, of the U.S. Air Force Office of Scientific Research, Aviation and Missile Research, Development, and Engineering Center, or the U.S. Government.

References

[1] Muramoto, K. K., "Algebraic Correlations for High-Speed Transition Prediction on Sharp and Blunt Cones," AIAA Paper 99-0405, 1999.

[2] Bertin, J. J., and Cummings, R. M., "Fifty Years of Hypersonics: Where We've Been, Where We're Going," *Progress in Aerospace Sciences*, Vol. 39, Nos. 6–7, Aug.–Oct. 2003, pp. 511–536. doi:10.1016/S0376-0421(03)00079-4

[3] Bouslog, S. A., An, M. Y., Hartmann, L. N., and Derry, S. M., "Review of Boundary Layer Transition Flight Data on the Space Shuttle Orbiter," AIAA Paper 91-0741, Jan. 1991.

[4] Lin, T. C., Grabowsky, W. R., and Yelmgren, K. E., "Search for Optimum Configurations for Re-Entry Vehicles," *Journal of Spacecraft and Rockets*, Vol. 21, No. 2, March–April 1984, pp. 142–149.

[5] Korejwo, H. A., and Holden, M. S., "Ground Test Facilities for Aerothermal and Aero-Optical Evaluation of Hypersonic Interceptors," AIAA Paper 92-1074, Feb. 1992.

[6] Hirschel, E. H., "Heat Loads in Hypersonic Vehicle Design," *Future Aerospace Technology in the Service of the Alliance*Vol. 3, Canada Communications Group, Ottawa, AGARD CP-600, 1997, pp. 235–243.

[7] Wright, M. J., Candler, G. V., and Bose, D., "Data-Parallel Line-Relaxation Method for the Navier–Stokes Equations," AIAA Paper 97-2046CP, June 1997.

[8] Johnson, H. B., and Candler, G. V., "Hypersonic Boundary Layer Stability Analysis Using PSE-Chem," AIAA Paper 2005-5023, June 2005.

[9] Reshotko, E., "Boundary Layer Instability, Transition, and Control," AIAA Paper 94-0001, Jan. 1994.

[10] Jaffe, N. A., Okamura, T. T., and Smith, A. M. O., "Determination of Spatial Amplification Factors and Their Application to Predicting Transition," *AIAA Journal*, Vol. 8, No. 2, Feb. 1970, pp. 301–308.

[11] Chen, F.-J., Malik, M. R., and Beckwith, I. E., "Boundary-Layer Transition on a Cone and Flat Plate at Mach 3.5," *AIAA Journal*, Vol. 27, No. 6, June 1989, pp. 687–693.

[12] Malik, M. R., "Hypersonic Flight Transition Data Analysis Using Parabolized Stability Equations with Chemistry Effects," *Journal of Spacecraft and Rockets*, Vol. 40, No. 3, May–June 2003, pp. 332–344.

[13] Horvath, T. J., Berry, S. A., Hollis, B. R., Chang, C.-L., and Singer, B. A., "Boundary Layer Transition on Slender Cones in Conventional and Low Disturbance Mach 6 Wind Tunnels," AIAA Paper 2002-2743, June 2002.

[14] Malik, M. R., Spall, R. E., and Chang, C.-L., "Effect of Nose Bluntness on Boundary Layer Stability and Transition," AIAA Paper 90-0112, Jan. 1990.

[15] Stilla, J., "Engineering Transition Prediction for a Hypersonic Axisymmetric Boundary Layer," *Journal of Aircraft*, Vol. 31, No. 6, Nov. 1994, pp. 1358–1364.

[16] Johnson, H. B., Seipp, T. G., and Candler, G. V., "Numerical Study of Hypersonic Reacting Boundary Layer Transition on Cones," *Physics of Fluids*, Vol. 10, No. 10, Oct. 1998, pp. 2676–2685. doi:10.1063/1.869781

[17] Schneider, S. P., "Flight Data for Boundary-Layer Transition at Hypersonic and Supersonic Speeds," *Journal of Spacecraft and Rockets*, Vol. 36, No. 1, 1999, pp. 8–20.

[18] Wadhams, T. P., MacLean, M. G., Holden, M. S., and Mundy, E., "Pre-Flight Ground Testing of the FRESH FX-1 at Flight Duplicated Conditions," AIAA Paper 2007-4488, June 2007.

[19] Saunders, D., Yoon, S., and Wright, M., "Approach to Shock Envelope Grid Tailoring and Its Effect on Reentry Vehicle Solutions," AIAA Paper 2007-207, Jan. 2007.

[20] Johnson, H. B., and Candler, G. V., "PSE Analysis of Reacting Hypersonic Boundary-Layer Transition," AIAA Paper 99-3793, June 1999.

[21] MacLean, M., Mundy, E., Wadhams, T., Holden, M., Johnson, H., and Candler, G., "Comparisons of Transition Prediction Using PSE-Chem to Measurements for a Shock Tunnel Environment," AIAA Paper 2007-4490, June 2007.

[22] Johnson, H. B., Seipp, T. G., and Candler, G. V., "Numerical Study of Hypersonic Reacting Boundary Layer Transition on Cones," AIAA Paper 97-2567, June 1997.

R. Kimmel
Associate Editor